Large acceleration of electrons by the microstructure of quasi-normal shocks

Charles Chiu and Wendell Horton
Institute for Fusion Studies, University of Texas at Austin, Austin, TX 78712
Yukiharu Ohsawa
Department of Physics, Nagoya University, Nagoya 464-8602, Japan

February 11, 2005

Abstract

Orbits of high speed test electrons are analyzed for their acceleration by quasi-normal shocks, where the parameters of the electromagnetic fields of the shocks are motivated by recent cluster mission data. Numerical simulations in this regime leads to the following two observations. First, for a given electron initial speed, by adjusting the quasi-normal angle the gyrating electron trajectory may be trapped along the shock front over a long range, and the electron may gain large energy. Second, this energy gain is predominantly associated with the kinetic energy parallel to the magnetic field. Based on a simple analytic model together with the nucleon-to-electron-mass (M/m)-scaled models, one may deduce an analytic expression which gives the maximum energy in terms of the optimal quasi-normal angle. The same approach also gives a understanding for the growth of the parallel kinetic energy. Since the ejected electron has a small pitch angle and thus follows the magnetic field line in the foreshock region. Simulation of electrons with uniform angular distributions on a fixed energy shell show that electrons from a substantial part of the shell acquire energies which are over one-half of the maximum energy. This suggests that quasi-normal shocks provide a mechanism to accelerate high-speed electrons to higher energy.

1 Introduction

The acceleration of charged particles in astrophysical and space plasmas has attracted a great deal of attention for many years. The highest energy of observed cosmic rays is $\sim 10^{20}$ eV [1]. Recent x-ray and gamma-ray observations have revealed that, in supernova remnants, electrons can be accelerated to $\sim 10^{14}$ eV [2, 3, 4] and ions to $\sim 10^{12}$ eV [5]. In the solar corona, solar flares can produce relativistic ions with $\sim 10^{10}$ eV and ultrarelativistic electrons with $\sim 10^{8}$ eV [6, 7, 8]. The acceleration of the solar energetic particles is very quick, less than a few seconds. The elemental composition of cosmic rays is, on average, similar to that of the universe [9, 10].

Intensive theoretical work on particle acceleration has also been made. In particular, particle simulations have shown that shock waves in a magnetized plasma can promptly accelerate particles (hydrogen ions, heavy ions, and electrons) with nonstochastic mechanisms to the energy level of solar energetic particles (see, for instance, Ref. [11], and references therein).

Earlier, we have developed [12] the details of the simulation of the Earth's magnetosphere as a magnetic obstacle in the plasma wind emitted from the sun which forms a plasma electrodynamic dynamo that accelerates charged particles. If an electron gyrating-trajectory is drifting along an electric field E_y, the energy which an electron acquires will be $\Delta K = eE_y\Delta y$. Our present work is to investigate the acceleration range, Δy, due to the microstructure of the collisionless shocks formed by interactions between solar wind and the local ambient magnetic field.

The most detailed measurements of the collisionless shock occurred from the CLUSTER mission were measurements [13, 14] on plasma density and magnetic field variations in the foreshock, bowshock and magnetosheath regions. The data shows that there are "short large amplitude magnetic structure" (SLAMS) forming the bow shock. Several hundreds of such structures were seen. They have different plasma properties depending on their location with respect to the magnetosphere.

The measurement on the properties of the fast magnetosonic shocklets at the bow shock [14] is relevant to our present investigation. In geocentric solar ecliptic (GSE) coordinates, the cluster satellites traveled from $(10, 3.8, -7.6)\, R_E$ to $(5, 0, -8)\, R_E$. For our present study, we will use the "solitary" structure data as a guide to adopt the parameters of the shock and the plasma for the present numerical work.

The solitary structure was moving toward the earth with a speed slower

than the solar wind. With respect to the plasma of the wind, this structure is moving toward the sun with a speed 210 km/s relative to the plasma. Upstream from the data gives the plasma density $n_0 \sim 2.2/\mathrm{cm}^3$, and the magnetic field $B_0 \sim 2\,\mathrm{nT}$. The corresponding Alfvén speed: $v_A = B_0/\sqrt{\mu_0 n_0 m_p} \sim 30\,\mathrm{km/s}$. The collisionless ion skin depth is $c/\omega_{pi} = 150\,\mathrm{km}$. At the shock front, there is a rise by a factor of 6 in the magnetic field to 12 nT. The half-width of the rise in B_z is $D \sim 50\,\mathrm{km}$. The sound speed is $c_s = 70\,\mathrm{km/s}$. This gives the proton temperature $T_p = Mc_s^2 = 50\,\mathrm{eV}$. For simplicity we assume the electron temperature, T_e is the same as the proton temperature, which leads to $\beta = n_0 T_e/(B_0^2/2\mu_0) \sim 11$, that is the structure is associated with a high-β plasma, which provides a source of high speed electrons.

We investigate the acceleration of high speed test-electrons, as they enter into the region of a quasi-normal shock, formed by the interaction between high-β plasma wind and a strong ambient magnetic field. Based on numerical simulations using the quoted shock parameters, we found that by tuning the quasi-normal oblique angle of the shock, the electron gyrating trajectory drifts over a large spatial interval along the shock front surface in the direction defined by $[-e\boldsymbol{v}^{pl} \times \boldsymbol{B}]$, where $\boldsymbol{v}^{pl}$ is the velocity of the plasma wind relative to the shock. Eventually the gyrating trajectory is reflected from the shock region moving toward upstream. This process leads to a substantial energy gain. We have developed a physical picture and a formula for the duration of the lingering process at the reflection. More specifically, we correlate the energy gain to the quasi-normal angle, and show analytically that there is a persistent transfer of the test electron transverse kinetic energy into its longitudinal kinetic energy. We show that the eventually reflected electrons are expected to move predominantly along the direction of the ambient magnetic field. This may remind one of earlier work on the acceleration of nonthermal relativistic ions discussed by Usami *et al.*; lingering near the shock front, increase in perpendicular kinetic energy, and energy transfer from perpendicular to parallel components [15, 16, 17]. On the other hand, the electron acceleration discussed in Ref. [18] will occur in a rather strong magnetic field such as in solar magnetic flux tubes and thus is not relevant to the present case.

We have also carried out a fixed energy shell simulation showing that a substantial fraction of electrons from the shell has acquired energies, which are over one-half of the maximum energy. We conclude that quasi-normal shocks with a sufficiently strong jump in the magnetic field will provide a mechanism to accelerate high-speed electrons to higher energies.

The remainder of this paper is organized as follows. In Sec. 2, the quasi-normal shock model formulated in terms of the dimensionless variables is discussed. In Sec. 3, numerical simulations are given. Analytic expression which estimates the total energy gain and the expression which determines the transfer of the transverse to longitudinal energy are discussed. In Sec. 4, we present the dependence of energy-gain factor on the polar and azimuthal angles on the fixed energy shell of the initial states. A summary and conclusions are given in Sec. 5. The present work is presented in the context of nonrelativistic formalism using quasi-normal approximation. Based on the work of Refs. [15, 16, 17] which considers shock acceleration of ions, a discussion for the electron case using the relativistic framework and general oblique angles is given in the Appendix.

2 Shock model

2.1 Quasi-normal shocks

We begin with the soliton solution in the two component cold fluids of electrons and protons [19, 20] A planar plasma wind with two component fluids is moving along the negative x-axis normal to an ambient magnetic field. The interaction between the plasma wind and the ambient field forms a normal shock. Denote θ to be the angle between the upstream magnetic field relative to the shock normal, $\boldsymbol{v}^{pl}$, where the plasma is moving along the negative x-direction and the magnetic field; $\theta = 90°$ for the present situation. One assumes field components depend only on x. As we shall see below, the Cartesian components of the soliton solution takes on the form:

$$\boldsymbol{B} = (0,\, 0,\, B_z(x)), \text{ and } \boldsymbol{E} = (E_x(x),\, E_{y0},\, 0). \tag{1}$$

Denote the electron mass, its velocity and the medium density by m, $\boldsymbol{v}$, and n, respectively. The corresponding ion quantities for the proton are m_i, n and $\boldsymbol{v}_i$. Here we have assumed quasi-neutrality, $n_i = n_e = n$. Along the x-direction $v_{xi} = v_{xe} \equiv v_x$. For brevity, the subscript "e" is suppressed. The subscript "0" will refer to quantities far away in the upstream region. Throughout this work, unless explicitly stated, we will always work in the rest frame of the shock, so the jump across the shock front is stationary. The continuity equation for the electrons in the shock frame implies that

$$v_{x0} n_0 = v_x n. \tag{2}$$

The Ampere's law, $\nabla \times \boldsymbol{B} = \mu_0 \boldsymbol{j}$, leads to

$$\frac{dB_z}{dx} = \mu_0 n e v_y \tag{3}$$

where the relation $j_y = -ne(v_y - v_{yi}) \approx -nev_y$ was used [19]. This is due to the fact that $v_{ye} \approx -(m_i/m_e)v_{yi}$ in perpendicular waves. For quasi-perpendicular waves where $\cos\theta \ll 1$, v_{ye} is expected continue to be much greater than v_{yi}. On the other hand, for oblique waves where $\cos\theta \sim O(1)$, v_{yi} and v_{ye} are of the same order.

The Faraday's law $\nabla \times E = -\partial B/\partial t$ leads to

$$\frac{dE_y}{dx} = 0, \text{ or } E_y = E_{y0}; \text{ and } \frac{dE_z}{dx} = 0, \text{ or } E_z = E_{z0} = 0, \tag{4}$$

in the wave frame. In the last step, we invoke the assumed boundary condition that in the wave frame in the upstream, $E_z = 0$. Because the electron mass is small, from the Lorentz force law one finds following relations,

$$E_x \approx -v_y B_z, \tag{5}$$

$$E_y \approx v_x B_z \equiv E_{y0} = v_{x0} B_{z0}. \tag{6}$$

Combining Eqs. (2), (3), (5), and (6), we obtain

$$E_x = -v_y B_z = -\left[\frac{dB_z/dx}{\mu_0 n e}\right] B_z = -\frac{B_{z0}}{\mu_0 n_0 e}\frac{dB_z}{dx}. \tag{7}$$

Here in the last step the relation $B_z/n = B_{z0}/n_0$ was used, which follows from the continuity relation Eq. (2) and Faraday law, Eq. (6). This relation was first derived in a soliton solution [19], which was subsequently demonstrated to hold for the damped soliton which may be regarded as a normal shock [20].

Now consider the oblique angle case, where the ambient magnetic field in the upstream region is in the x-z-plane with $B_x = B_0 \cos\theta$ and $B_z = B_0 \sin\theta$. For the quasi-normal shock, we will be concerned with the case where $\cos\theta \ll 1$. From the magnetic gauss law: $\nabla \cdot B = 0$,

$$\frac{dB_x}{dx} = 0, \text{ or } B_x = B_{x0} \equiv B_0 \cos\theta. \tag{8}$$

Here the Cartesian components of the fields in the quasi-normal shock region is expected to take the form:

$$\boldsymbol{B} = (B_{x0}\, B_y(x),\, B_z(x)), \text{ and } \boldsymbol{E} = (E_x(x),\, E_{y0},\, 0). \tag{9}$$

We assume the x-dependences of field components of a normal shock may also be valid for the quasi-normal shock. Thus except for B_y, all other field components are now given. The electric field components given are

$$E_x(x) = -\frac{B_{z0}}{\mu_0 n_0 e} \cdot \frac{dB_z}{dx},\ E_{y0} = -v^{pl} B_{z0}, \tag{10}$$

and the magnetic field components are

$$B_{x0} = B_0 \cos\theta,\ \text{and } B_z(x) \text{ with } B_{z0} = B_0 \sin\theta. \tag{11}$$

Here v^{pl} is the relative velocity of the plasma wind moving along the negative x-direction with respect to the shock front located near the origin.

Now we come to $B_y(x)$. From both numerical simulation and space craft observation, there is strong evidence for the presence of B_y associated with the structure of oblique angle shocks [21]. Intuitively the existence of this component may be associated with the condition that there is no current flowing in the asymptotic post shock region. For a historical account of early controversies [22, 23, 24] and an expression of an x-integral over B_y see Ref. [25]. See also a recent discussion on related topics where this integral form is quoted[26].

We would like to show that B_y may readily be obtained with an expression, which is the same as the differential of the integral mentioned above, based on Eqs. (5-7) together with the relation

$$(v_x B_y - v_y B_x) \approx -E_z = 0,\ \text{thus } B_y = \frac{v_y}{v_x} B_x. \tag{12}$$

The first equation follows from the z-component Lorentz force law when the electron mass is neglected and the present boundary condition where $E_z = 0$.

From the x-component and the z-component of the Lorentz force law, Eqs. (5, 12), B_y and E_x are related to the electron velocity v_y. This implies that there is a constraint between these two field components. By eliminating v_y between Eq. (5), and Eq. (12), one obtains

$$B_y = -\frac{E_x B_x}{v_x B_z} = -\frac{E_x B_{x0}}{v_{x0} B_{z0}} = -\frac{\cot\theta}{v^{pl}} E_x = \frac{1}{v^{pl}} \cdot \left[\frac{B_{x0}}{\mu_0 n_0 e}\right] \frac{dB_z}{dx}. \tag{13}$$

For the third to the last step, Eqs. (6) and (8) were used. For the next step $B_{x0}/B_{z0} = \cot\theta$ was used. Using the notation introduced above, the

upstream fluid velocity $v_{x0} \equiv v^{pl}$. In the last step Eq. (7) was used. The last expression is the differential version of the integral expression of Eq. (10) given in Ref. [25].

Our equations: (9), (10), (11), and (13) define the present quasi-normal shock model. Only the fluid velocity retained is the plasma wind velocity defined relative to the shock, v^{pl}. We will proceed to investigate the motion of test particles in the presence of all field components: (E_x, E_y; B_x, B_y, B_z) of the shock. The latter are now treated as the external fields acting on these test particles. This set of field components was derived earlier for general oblique angle magnetosonic waves based on the reductive perturbation method [28, 29, 30] by one of us (YO) [27]. This perturbation theory includes the effect of finite temperature. In addition, the general component fields given above have also been confirmed through PIC simulation [15, 16, 17, 18].

The present quasi-normal shock model is defined by the field components specified by Eqs. (9-11) and Eq. (13). The only fluid flow velocity enters in the definition of field components is v^{pl}, which is the relative velocity of the upstream fluid with respect to the shock. It is this set of field components which will play the role of external fields interacting with test particles.

We will be in the kinematic region where the test electron speed is much larger than the shock propagation speed. We shall see that in this region the effect of E_x is relatively unimportant. Also in quasi-normal approximation, B_y is suppressed by a $\cos\theta$ multiplicative factor. For our investigation on the effect on the energy gain factor due to local field components, we consider following two models.

- Model-I: We model with a simplified case, only the upstream finite fields B_z and B_{x0}, and the dynamo field E_{y0} are kept.

- Model-II: In addition to those field components of model-I, the field components E_x and B_y are included. The latter are proportional to dB_z/dx, and thus they are "local fields." We will investigate the effect of local fields on the energy gain. As we will see in the kinematic region of present interest, the effect is relatively small.

2.2 Lorentz force equation and dimensionless variables

The motion of an electron is governed by the Lorentz force equation:

$$m\frac{d\boldsymbol{v}}{dt} = -e(\boldsymbol{E} + \boldsymbol{v} \times \boldsymbol{B}). \tag{14}$$

We work with the dimensionless spatial and time variables, with the length scaled by the ion collisionless skin depth c/ω_{pi}, and the time scaled by the inverse of the ion gyro-frequency, i.e., $x = c\xi/\omega_{pi}$ and $t = \tau/\omega_c$. Here $\omega_{pi} = (n_0 e^2/\epsilon_0 M)^{1/2}$ and $\omega_c \equiv \omega_{ci} = eB_{z0}/M$. The plasma density n_0 and the magnetic field B_0 are defined in front of the shock. Protons are used for the plasma ions and M is the proton mass. The velocity variable is scaled by the Alfvén speed: $v_A = (c/\omega_{pi})\omega_c = B_0/\sqrt{\mu_0 n_0 M}$.

Denote the dimensionless magnetic field $b = B/B_0$. The dimensionless gyro-radius, gyro-frequency and gyro-period may be introduced respectively in the following way:

$$r_e = \frac{v_\perp}{\omega_{ce}} = \frac{u_\perp v_A}{\frac{M}{m} b\omega_c} \equiv \rho_e \left[\frac{c}{\omega_{pi}}\right], \text{ with } \rho_e = \frac{m u_\perp}{M b} \tag{15}$$

$$\omega_{ce} = \frac{eB}{m} = \left(\frac{qB_0}{M}\right)\frac{Mb}{m} \equiv \Omega_e[\omega_c], \text{ with } \Omega_e = \frac{M}{m} b. \tag{16}$$

$$t_e = \frac{2\pi r_e}{v_\perp} = \frac{2\pi \rho_e \frac{c}{\omega_{pi}}}{u_\perp v_A} = \frac{2\pi\rho_e}{u_\perp}\cdot\frac{1}{\omega_c} \equiv \tau_e\left[\frac{1}{\omega_c}\right], \text{ where } \tau_e = \frac{2\pi}{b}\frac{m}{M}. \tag{17}$$

The dimensionless kinetic energy

$$K_e = \frac{1}{2} m v^2 = \frac{1}{2} u^2 v_A^2 \equiv k_e[mc^2], \text{ with } k_e = \frac{u^2\beta_A^2}{2}. \tag{18}$$

The work done on an electron by an electric field E_y over a range Δy, which is also the energy gain, is given by

$$W_e = qE_y\Delta y = q(e_{y0} v_A B_0)\left(\Delta\xi_y \frac{c}{\omega_{pi}}\right) \equiv w_e\left[mc^2\right], \tag{19}$$

with the dimensionless work done by the y-component electric field over a range $\Delta\xi_y$: $w_e = (M/m)e_{y0}\Delta\xi_y\beta_A^2 = e_{y0}\Delta\xi_y B_0^2/(\mu_0 n_0 m c^2)$.

Quantities ρ_e, Ω_e, t_e, k_e and w_e are dimensionless quantities. Those in the square brackets are respective dimensional units. In terms of the Cartesian components, the dimensionless Lorentz equation is given by

$$\begin{pmatrix} du_x/d\tau \\ du_y/d\tau \\ du_z/d\tau \end{pmatrix} = \begin{pmatrix} -e_x M/m - (u_y\Omega_z - u_z\Omega_y) \\ -e_{y0}M/m - (u_z\Omega_{x0} - u_x\Omega_z) \\ -(u_x\Omega_y - u_y\Omega_{x0}) \end{pmatrix}. \tag{20}$$

Here u_i is the ith component of the dimensionless velocity where the subscript $i = x$, y, or z, $u_i = v_i/v_A$ and Ω_i is the electron gyro-frequencies, $\Omega_i = Mb_i/m$. This is for model-II. For model-I, the terms involving local field components e_x and $b_y(x)$ (or Ω_y) are absent.

2.3 Parameterization of the field components

The dimensionless fields are defined by $\boldsymbol{b} = \boldsymbol{B}/B_0$ and $\boldsymbol{e} = \boldsymbol{E}/(v_A B_0)$. From Eq. (9),

$$\boldsymbol{b} = (b_{x0},\, b_y,\, b_z) \text{ and } \boldsymbol{e} = (e_x,\, e_{y0},\, 0). \tag{21}$$

We will continue to use the convention, that the script "0" is used for quantities in front of the shock, and "1" within the shock. By definition, $b_0 = 1$, then $b_{x0} = \cos\theta$, since b_x is constant, $b_{x1} = b_{x0}$. The magnetic field b_z is assumed to have the form of the damped soliton solution, which is approximately given by

$$b_z(\xi) = 1 + \frac{b_1 - 1}{2}\left[1 - \tanh\left(\frac{\xi}{d}\right)\right]. \tag{22}$$

Here the thickness of the transition layer is $2d$. In the quasi-normal approximation, $b_{z1} \approx b_1$, so the jump of b_z is $\sim (b_1 - 1)$. In the context of the soliton solution, the corresponding dimensionless electric field is

$$e_x = -\frac{db_z}{d\xi} = \frac{b_1 - 1}{2d}\mathrm{sech}^2(\xi/d). \tag{23}$$

We explain that e_x is always positive as to accelerate cold electrons into the ion layer to reduce the charge separation. The above calculations, i.e., Eqs. (5)-(7), and (23), are based on a cold plasma model; the thermal pressure has been neglected compared with the magnetic pressure. In a cold plasma, the parallel electric field $E_\parallel$ is weak, which can be seen from the relation between $E_\parallel$ and the density perturbation n_1,

$$eE_\parallel = -\frac{T_e}{n_0}\frac{\partial n_1}{\partial s}, \tag{24}$$

where T_e is the electron temperature, and s is the length along the magnetic field [32]. This, however, does not mean that the longitudinal electric field E_x is weak. It means that the total electric field consisting of the longitudinal

and transverse components is nearly perpendicular to the magnetic field (E_x given by Eq. (7) is generated by the charge separation across the magnetic field, which arises from the difference in ion and electron masses [27]). In high beta plasmas, on the other hand, the longitudinal electric field is dominated by the one caused by the electron thermal pressure [27]. In this case, we have $E_{\parallel} \sim E_x \cos\theta$.

For later reference, based on Eq. (13) the dimensionless y-component magnetic field is given by

$$b_y(x) = \frac{\cos\theta}{u^{pl}} \frac{\partial b_z}{\partial \xi} = -\frac{\cos\theta}{u^{pl}}\ e_x(x). \tag{25}$$

2.4 M/m scale invariance and breaking of invariance.

In the dimensionless Lorentz force equation: Eq. (20), one may scale the time by defining the new variable $\tau^* = \tau \cdot M/m$. This would then lead to a M/m-scale invariant theory, except for the length parameter d in the shock structure of the fields, which breaks the M/m scale invariance.

We shall see that the electron trajectory can be investigated analytically in a step function approximation for the ramp of the field B_z. In this limit the M/m scale invariance is recovered. Suppose now we consider the situation with some fixed finite width d and fix the nucleon mass M. As the ratio M/m is decreasing, the electron momentum is increasing. In turn the electron gyroradius $\rho_e = mu_{\perp}/Mb$ is increasing. When thickness of the shock is fixed, the relevant scale breaking parameter is d/ρ, which is now decreasing. If d/ρ is sufficiently small, the numerical simulation model will be approximately the step function model. The model with such M/m ratio may be used as a benchmark case to be compared with predictions based on analytic step-function case. It turns out that the $M/m = 20$ case satisfies this criterion. This case can be used to compare with the analytic model. On the other hand by varying the M/m ratio, we can see how features in the M/m are involved to the physical case where $M/m = 1800$.

For the numerical work presented below, we will be mainly comparing the model predictions for the $M/m = 20$ case and those of the $M/m = 1800$ case. Some information of the intermediate case with $M/m = 200$ will be included to indicate the trend of M/m-dependence.

We will see that as the ratio of M/m increases, the M/m scale-breaking effect sets in most prominently in the variation of the optimal angle, where

the angle is between the shock normal and the upstream magnetic field vector. In particularly starting from $M/m = 20$, as this ratio increases, there is graduate decrease in this optimal angle and a corresponding decrease in maximum energy.

3 Simulation results and analytic results

3.1 SLAMS motivated parameters

Our investigation involves both numerical simulation and analytical work. For the simulation part, we use following shock parameters based on the event in the SLAMS data reported in Stasiewicz *el al.* [14] mentioned earlier. The relative velocity between the magnetopause plasma and the shock is taken to be $v^{pl} = -7v_A$, where $v_A = 30\,\mathrm{km/s}$ as implied by the ambient field $B_{z0} = 2$ nT and the electron density $n_0 = 2.2/\mathrm{cm}^3$. Here the minus sign denotes the plasma flow is away from the sun. The proton sound speed is $c_s = 70\,\mathrm{km/s}$, assuming the electron temperature, $T_e = (1/2)mv_e^2$, is the same as the proton temperature, 50 eV, the corresponding electron thermal speed is $v_e = \sqrt{2M/m_e} \approx 4200\,\mathrm{km/s} \approx 140v_A$.

It is well known that trajectory tracing is a parameter-sensitive enterprise. A slight change of some relevant parameter, could lead to quite a different trajectory, which could lead to a different amount of energy gain. In the present work, recognizing that there is a maximum in the energy gain factor in the quasi-normal region, we adopt following two-step strategy. In the first step we fix all the parameters of the problem, say based on the SLAMS data, except for the oblique angle θ. We determine the optimal angle, which leads to a maximum in the energy gain, i.e. $K_f - K_0 = \mathrm{Max}(W_e(\theta))$, with W_e defined in Eq. (19). In the second step, we do a fixed energy shell calculation to obtain the energy gain factor distribution as a function of the orientation of the initial velocity vector of the test particle within the shell.

We assume the test electron velocity distribution is isotropic in the rest frame of the upstream plasma. Among those isotropic points on the fixed energy shell, we work with the case of where the test electron is initially moving toward the shock with a speed relative the shock $v_{x0} \equiv u_{x0}v_A = -147v_A$. At the shock front, as mentioned earlier the rise of the magnetic field in the SLAMS event is over about 100 km. The dimensionless half width $d = 50\,\mathrm{km}/(150\,\mathrm{km}/(c/\omega_{pi})) \sim 0.3c/\omega_{pi}$. Hereon unless explicitly stated, the

length units is c/ω_{pi}. We will also use the convention $c/\omega_{pi} = 1$, and write $d \sim 0.3$.) This is to be compared with the upstream side electron gyro-radius $r_e = m_e u_\perp / eB_0 \sim 12\,\mathrm{km} \sim 0.08 c/\omega_{pi}$. The jump of B_z is from the ambient value of 2 nT to 12 nT. The corresponding dimensionless fields are taken to increase from $b_0 = 1$ to $b_1 = 6$ across the shock front.

Below we discuss two cases, the "physical case," where $M/m = 1800$, and the "M/m-scaling limit case," essentially the case with a step function at the shock front. For the latter case, it is adequate to work with $M/m = 20$. By comparing simulation results of model-I and model-II, we investigate the effects of the local fields, E_x and B_y.

3.2 Simulation of model-II: $M/m = 1800$ and $M/m = 20$

Figure 1 illustrates the projection of trajectory of the test electron in the x-y-plane for the physical case where $M/m = 1800$ and $d = 0.3$. Model-II, which includes all field components, is used here. To understand the shape of the trajectory shown, we find it is instructive to first describe a simpler shape, i.e., for the $M/m = 20$, Model-I case, where the trajectory consists of essentially 3 sides of a rectangle. This is depicted in Fig. 2. The trajectory begins with a left-going drift. This corresponds to the first side of the rectangle. As the gyrating-orbit first touches the $x = 0$ line, where B_z jumps from B_0 to B_1, there is a clockwise 90° turn in the drift (see the zoom-in view in Fig. 2d) which leads to a drift along the shock front, in the positive y direction. This along the shock front drift is accompanied by a gradual shift in the x-direction. First there is the slowing down of the shift to the downstream side (left). The zoom-in view at the around mid-way is shown in Fig. 2c. Here $\xi_x < -d = -0.3$, i.e., x goes beyond the ramp into the negative x-region. As the y-drift approaches and passes the midway point, the x-drift to the left slows down to a stop and then turns around begins to shift to the right with an increasing speed, slowly but steadily. In this manner, the trajectory continues drifting upward for some distance while it is persistently being shifted to the right. This upward drift constitutes the second side of the rectangle. As the gyrating orbit leaves the $x = 0$ line, there is another 90° clockwise rotation. (For the zoom-in view see Fig. 2b). Here the x-drift reaches its final right moving speed. Beyond this point the x-drift becomes the main drift moving to the right, which is the third side of the rectangle.

The trajectory shape for the $M/m = 1800$ case depicted in Fig. 1 which

is somewhat similar to the $M/m = 20$ case, the essentially scaling limit case just described, except that the two sharp 90° corners are replaced by the round corners and also the important difference in the y-range. From the overview plot (Fig. 1a) and the zoom in views of Fig. 1b, 1c and 1d, one sees that most of the bending at both the upper and lower corners occur within $\xi_x = 0.6 = 2d$. Most of the y-drift is within the interval $-0.1 < \xi_x < 0.3 = d$. In other words the bulk of y-motion is confined to within half width of the ramp. During the y-drift, the electron stays essentially on the ramp.

To the extent that the effect due to e_x can be neglected, the energy gain $K_f - K_0$ is given by the work done due to the y-component electric field over the relevant y-range: $\Delta\xi_y$. Once this range is given, based on Eq. (19), the energy gain factor can be determined in the following manner.

$$G_\xi \equiv \frac{K_f}{K_0} = \frac{w_e}{K_0} + 1, \text{ with } w_e = K_f - K_0 = \frac{M}{m} e_{y0} \Delta\xi_y \beta_A^2. \tag{26}$$

The simulation outputs of the optimal oblique angle, the y-range, the energy gain factors obtained from model-II simulation, G_{II}, and the calculated G_ξ factor are respectively given by

- $M/m = 1800 : \theta = 88.3°, \Delta\xi_y = 8.8$,or 1.3×10^3km, $G_{II} = 10.9$,$G_\xi = 11.2$.
- $M/m = 20 : \theta = 88.7°, \Delta\xi_y = 1370$, or 2.1×10^5km, $G_{II} = 18.7$,$G_\xi = 18.8$.

There is agreement between G_{II} and G_ξ for each M/m case to within a few percent. This indicates the level of agreement expected. It also suggests that the fact that the effect due to e_x on the gain factor is a most a few percent.

For the same electron initial velocity, the gyro-radius of the $M/m = 20$ case is 90 times greater than that of the $M/m = 1800$ case. For $M/m = 1800$ case, the SLAMS event gives $D = 50$ km, and the upstream side electron gyro-radius $r_e = m_e u_\perp / eB_0 \sim 12\,\text{km}$, or $(d/\rho)_{1800} \sim 4$. The decrease in the optimal angle for the $M/m = 1800$ case is attributed to be due to M/m-scale breaking, which leads to the corresponding decrease in G. We include below an intermediate case to indicate the trend of the decrease of the optimal angle as M/m increases.

- $M/m = 200 : \theta = 88.55°, \Delta\xi_y = 110$ or 1.7×10^4km, $G_{II} = 14.8, G_\xi = 15.3$.

On the other hand for $M/m = 20$ case, the inequality $(d/\rho)_{20} \sim 0.04 \ll 1$, and in turn the step function approximation is satisfied. In the next subsection we proceed with the analytic work to develop a formula to explain the energy gain factor.

3.3 Average acceleration in the shock normal-direction and the total energy gain

To determine the gain in kinetic energy, or equivalently the range of y-drift, we first investigate the average acceleration along the shock normal direction, i.e. the x-direction. The Lorentz force equation Eq. (20), neglecting e_x-term, which is justified for the high-β case we are considering, also due to the fact that e_x is a conservative field the effect of e_x does not accumulate [15, 16, 17], leads to

$$\frac{d^2 u_y}{d\tau^2} \approx -u_y \Omega_y^2, \text{ or } u_y = u_\perp \cos(\Omega_y \tau - \phi), \tag{27}$$

where $\Omega_y^2 \equiv \Omega_{x0}^2 + \Omega_z^2$. Consider the situation of a typical gyro-cycle depicted in Fig. 3 along the path: PDAB'P'. Along PDA, which is to the left of the $x = 0$ line, we denote u_y by u_y^L. Here

$$\Omega_y \approx \Omega_1 = \left(\frac{M}{m}\right) b_1. \tag{28}$$

Along AB'P', denote u_y by u_y^R, where

$$\Omega_y \approx \Omega_0 \approx \left(\frac{M}{m}\right) \left[1 + (\cot\, \theta_0)^2/2\right]. \tag{29}$$

The average x-acceleration per cycle is given by

$$\begin{aligned}
\langle a_x \rangle &= -\left\langle \Omega_{z1} u_y^L \right\rangle_{PDA} - \left\langle \Omega_{z0} u_y^R \right\rangle_{AB'P'} \\
&= -\frac{u_\perp}{T} \left[\int_{\tau P}^{0} \Omega_{z1} \cos(\Omega_1 \tau - \phi) d\tau + \int_{0}^{\tau P'} \Omega_{z0} \cos(\Omega_0 \tau - \phi) d\tau \right] \\
&\approx -\frac{u_\perp}{T} \left[-2 \sin\phi + (1-\epsilon)(\sin(\phi + 2\epsilon\phi) + \sin\phi) \right] \\
&\approx (\cot\theta)^2 \frac{u_\perp}{T} f(\phi), \text{ where } f(\phi) = \sin\phi - \phi\cos\phi.
\end{aligned} \tag{30}$$

In the second step, the limits of the two integrations are as follows. The time at A is zero. The time at P and at P' are respectively $\tau_P = -2\alpha/\Omega_{z1}$ and

$\tau_{P'} = 2\phi/\Omega\, z0$. Here the solutions for $x < 0$, $u_y = u_y^L$ and for $x > 0$, $u_y = u_y^R$ were used. In the third and the fourth steps, the small epsilon approximation of Eqs. (28) and (29) were used. The acceleration in Eq. (30) is the large gyro-radius analog of the mirror force for the small gyro-radius cold electrons due to the increase in $B_z(x)$ throughout the shock.

The averaged acceleration is a function of ϕ. In the y-drift region, ϕ varies from π to smaller positive angle then back to π. To describe the x-drift in terms of some effective acceleration, we have made following simplifying assumptions. The effect of $f(\phi)$ contribution is presented by: $\overline{f} = f(\phi_{\text{eff}})$. We have assigned a typical period $T = T_1$ for gyro-cycles, and typical speeds: $\overline{u}_\perp$, for the tangential speed along the path of gyration, and $\overline{u}_y$, for the y-drift motion. From their definitions, $\overline{u}_\perp/\overline{u}_y \equiv \rho_0\Omega_0/(2\rho_0/T_1) = [M/(2m)]T_1$. Based on Eq. (30), the effective cycle-averaged acceleration becomes,

$$\langle a_x \rangle_{\text{eff}} = \frac{(\cot\,\theta)^2}{T_1} \cdot \left(\frac{M}{2m} T_1 \overline{u}_y\right) \overline{f} = (\cot\,\theta)^2 \overline{f} \overline{u}_y \cdot \frac{M}{2m}. \tag{31}$$

The following picture associated with the cycle averaged x-drift motion emerges. Before the y-drift, the gyro-center has the initial velocity of the plasma, so the initial x-drift velocity is u^{pl}, which is along the negative x direction. During the y-drift, the x-drift is governed by the effective acceleration given here. Along the x-direction, it slows down, turns around and causes the acceleration of the x-drift motion in the positive x-direction. Inspection on the motion in Fig. 3 reveals that within each gyro-cycle, to the extend that one ignores the slight change of transverse kinetic energy along the left hand side arc where the gyro-radius is relatively small, there is an approximate "elastic bounce" at each cycle. At the exit end of the y-drift, the x-drift velocity does not deviate far from $-u^{pl}$, moving along the positive x direction. We digress to comment that, as depicted in Figs. 1d, 1b, 2d and 2b, for each of the $M/m = 20$, and 1800 cases, the gyro-radius in the upstream region at the entrance end and that at the exit end are comparable. Using Eqs. (30) and (31) and the initial dimensionless kinetic energy: $K_0 = 0.5 u_0^2 \beta_A^2$ with $u_0 \equiv u_{0x}$, the total y-drift range is given by

$$\Delta\xi_y = \frac{\overline{u}_y \cdot 2u^{pl}}{\langle a_x \rangle_{\text{eff}}} = \frac{4}{\overline{f}} \cdot \frac{m}{M} \cdot \frac{u^{pl}}{(\cot\,\theta)^2}. \tag{32}$$

Neglect the e_x-contribution. From the Lorentz force law, Eq. (20), and

Eq. (19), the total energy increase can be written as

$$K_f - K_0 \approx \left(\frac{M}{m}\right) e_{y0} \Delta\xi_y \beta_A^2. \tag{33}$$

Using Eqs. (32) and (33) and $K_0 = u_0^2 \beta_A^2/2$, where $u_0 = u_{x0}$, the energy multiplication factor at the optimal angle becomes:

$$G_\theta \equiv \frac{K_f}{K_0} = 1 + \frac{M}{m}\frac{e_y \Delta\xi_y}{(u_0^2/2)} = 1 + \frac{8}{\overline{f}}\left(\frac{u^{pl}}{\cot\,\theta\, u_0}\right)^2 \sim 1 + 4\left(\frac{u^{pl}}{\cot\,\theta\, u_0}\right)^2. \tag{34}$$

In the last step we set $\overline{f} \sim 2$, which has been obtained by fitting several simulation results, where $2 < b_1 < 7$ and $0.001 < d < 0.5$. The value $\overline{f}$ here turns out to be the arithmetic mean of $f(\pi) = \pi$ and $f(\pi/2) = 1$. It is gratifying that $\overline{f}$ obtained is within the expected range.

Below is a comparison of the energy gain factor determined based on Eq. (34), G_θ, and the simulation results: G_I of model-I and G_{II} of model-II.

- $M/m = 20$: $\theta = 88.7°$, $G_\theta = 18.6$, $G_I = 18.8$, $\Delta_\theta G/G_I \sim 1\%$, $G_{II} = 18.7$.
- $M/m = 200$: $\theta = 88.55°$, $G_\theta = 15.2$, $G_I = 14.8$, $\Delta_\theta G/G_I \sim 2\%$, $G_{II} = 14.8$.
- $M/m = 1800$: $\theta = 88.3°$, $G_\theta = 11.3$, $G_I = 10.8$, $\Delta_\theta G/G_I \sim 4\%$, $G_{II} = 10.9$.

Accepting the fitted value of $\overline{f}$, the agreement is at a percent level. The last item on the list, $\Delta_\theta G/G_I = |G_\theta - G_I|/G_I$, shows the percent deviation between model-I from the step-function approximation for the ramp of B_z. As the ratio M/m increases, the M/m scale breaking is increasing, this percentage deviation is expected to increase. On the other hand, since the percent deviation is relatively small, it suggests that the quantity $\overline{f}$ is approximately M/m-scale invariant.

Comparison between G_I and G_{II} for all three cases indicate that the two extra local fields E_x and B_y included in model II have small effect on the total energy gain, although as we shall see below, that there some noticeable differences in the time curves of kinetic energy vs. time from the local fields.

We include here a discussion on the angular dependence of the energy gain factor which is illustrated in Fig. 4. The situation of $M/m = 20$ case

is shown on the left column. Fig. 4a shows a comparison between the curve, which is the analytic form of the gain factor G_θ given in Eq. (34) and the crosses, which are model-II simulation gain factors. As θ increases toward $90°$, the energy gain factor is steadily increasing until it reaches the critical angle, θ_{cr} where the gain factor peaks at the maximum value followed by an abrupt drop. This occurs when the shock front is no longer able to reflect the electron. Here there is an abrupt drop in the range of y-drift, in turn an abrupt drop in the energy gain factor.

In our numerical calculation, we determined the critical angle only approximately. This approximately determined critical angle will be referred it as the optimal angle, where the gain factor is close to the maximum value. Figure 4b is an enlarged view of the angular dependence of G near the critical angle region. The corresponding angular dependence of the total number of cycles in the y-drift region is shown in Fig. 4c. As the gyration cycles increases, y-range increases, in turn the increase in the energy gain. The angular dependence of the energy gain factor for $M/m = 1800$ is shown in Fig. 4d and Fig. 4e. The M/m-dependence of the number of gyro-cycles in the y-drift region vs. M/m at the optimal angle is shown in Fig. 4g. Notice the linear behavior of the curve.

Back to Fig. 4b and Fig. 4. For both M/m cases illustrated, at around $\theta = 87°$, there is about a factor of 4 drop in the gain factor. This leads us to define the quasi-normal region of the present interest to be where $\theta > 87°$ or $\cos\theta < 0.05$.

3.4 Temporal evolution of total, parallel and transverse kinetic energies

Now we turn our attention to the time evolution of the total, transverse and the parallel kinetic energy. Figures 5a and 5b illustrate the situation for $M/m = 1800$, for model-I and model-II respectively. In particular, in both cases there is a persistent increase in the parallel component of the kinetic energy and the final energy is dominated by this parallel component. In this section we will analyze the growth of the parallel component kinetic energy analytically using the step function approximation and will compare the analytic approach with the simulation results for $M/m = 20$, where the left column plots: Figures 5c, 5e and 5g are for model-I and the right column plots: Figures 5d, 5f and 5h, for model-II.

From the Lorentz force equation, the parallel component equation of motion can be written as

$$\frac{du_\parallel}{d\tau} = \frac{d}{d\tau}\left(u_x \cos\theta + u_z \sin\theta\right) = -e_x \frac{M}{m}\cos\theta + u_y(-\Omega_z \cos\theta + \Omega_{x0}\sin\theta) \approx 0. \tag{35}$$

The last step is valid away from the ramp region, where the parenthesis in the second equality is exactly zero. In practice the ramp region may be defined by $|\xi_x| < d \sim 0.3c/\omega_{pi}$.

We will first discuss the situation of model-I. Figure 5e is the zoom-in view of x vs. t, with the corresponding $K_\parallel$ vs. t shown in Fig. 5g. Inspection on Fig. 5e reveals that near $x = 0$, a full width $\Delta x = 2dc/\omega_{pi} = 0.6c/\omega_{pi}$ corresponds to a time interval $\Delta t < 0.01\omega_c^{-1}$. Away from the ramp region, the $K_\parallel$ time-curve should be flat.

The flat-segments are present in Fig. 5g where the corresponding x-variation is shown in Fig. 5e. Here the flat segments are separated by thick and thin vertical lines at specific times. Each thick vertical line is located at the time when the trajectory crosses a $x = 0$ point entering into the shock region, i.e. into the down stream region. Consecutive entry points are labeled by P, P' ..., where the same notation of the point entry is used in Fig. 3. Each thin vertical line indicates the time when the trajectory crosses $x = 0$ point, exiting the shock region, i.e. into the upstream region. The partitioned flat segments lead to an overall pattern: (ramp)–(upstream-flat-segment)–(ramp)–(downstream-flat segment)–(ramp) .... In general the widths of the flat segments may vary depending on the location of the gyro-orbit with respect to the line $x = 0$. There are times where the orbit barely touches the $x = 0$ line with the main part of the orbit in the upstream region. There are times where the orbit is mainly in the downstream region. We will see below that for model-I, the jumps are positive definite and adjacent jumps are comparable in values. This leads to a"mixed staircase pattern," or in short a "staircase" pattern as shown in Fig. 5g.

From Eq. (35), the jump across the shock layer at the point P in Fig. 3 is given by,

$$\delta u_\parallel^P = u_x^P(\cos\theta_1 - \cos\theta_0) + u_z^P(\sin\theta_1 - \sin\theta_0). \tag{36}$$

and at the exit point A,

$$\delta u_\parallel^A = -u_x^A(\cos\theta_1 - \cos\theta_0) - u_z^A(\sin\theta_1 - \sin\theta_0). \tag{37}$$

In the quasi-normal approximation, the second term in each of the two equations above is relatively small and may be neglected. These two expressions may be combined in the following manner. Using $u_x = u_\perp \sin\phi$, we write

$$\delta u_\parallel \equiv u_\parallel^f - u_\parallel^i \approx u_x(\cos\theta_f - \cos\theta_i) \approx |\theta_f - \theta_i| u_\perp \sin\phi > 0, \qquad (38)$$

with "f" and "i" labeling the initial and final points. Here $\cos\theta = b_x/b \ll 1$. We recall, $\nabla \cdot B = 0$, implies that $b_x = b_{x0}$, i.e., there is no jump in the numerator, b_x. It follows that the stronger is the field, the closer is the pitch angle to 90°, or the smaller is $\cos\theta$. As the point $x = 0$ is crossed for both entrance and the exit cases, the product $u_x(\cos\theta_f - \cos\theta_i)$ is always positive definite. For the entrance case, the sign of this product is $(-)(-) = +$ and for the exit case, $(+)(+) = +$. It follows that the jump associated with crossing the $x = 0$ line from either side is positive. Furthermore, in the step function model at $x = 0$, the magnitude $|\cos\theta_f - \cos\theta_i| = |b_{x0}(b_f^{-1} - b_i^{-1})|$ takes on the same value when the electron is either entering or leaving the shock region. In the y-drift region, at $x = 0$, the magnitude $|u_x| = u_\perp |\sin\phi|$ is a slowly varying sequence as the electron crosses this point back and forth successively. Thus Eq. (38) implies that those adjacent jumps should have comparable heights leading to the staircase pattern mentioned above.

Next we turn to the case of $M/m = 20$ and model-II, i.e. the corresponding plots in the right column: Figures 5d, 5f and 5h. Figure 5d shows the model-II prediction of $K_{\rm tot}$, $K_\parallel$ and K_T vs. t. The parallel kinetic energy of model I, the $K_\parallel^I$ curve, is included for comparison. One sees that although at the final time the parallel kinetic energies of model I and model II are comparable, the time taken to arrive at the same final for the two cases are different. It arrives at the final value sooner for model-I.

The zoom in view of x vs. t and $K_\parallel$ vs. t are given in Figs. 5f, 5h, for the time interval $t = 10$ to 10.2. Notice the presence of spikes in the ramp regions, which can be traced due to the B_y-term. Away from the ramp regions there are flat segments. Unlike the model-I case, here the rise of the level height occurs mainly at the entrance point, and there is more variation in the rise associated with the exit point in with the upstream region. The amount of rise here varies from one part of the trajectory to the next, and to the next. As indicated by Fig. 5d, that the cycle-averaged rate of increase over the entire y-acceleration region for the two models are very similar at least up to $t = 7$. Also by comparing the energy values between (c) and (d) at the final energy, one sees that the effect due to the presence of E_x and B_y on the final kinetic energy components is relatively small.

Finally the total kinetic energy is the sum of the transverse plus parallel kinetic energy. To the extent that we ignore the e_x-term, the building up of the parallel kinetic energy across the $x = 0$ line is supplied by the work done in y-direction. During each cycle, the transverse kinetic energy gets a boost from e_y. During each cycle, as the trajectory passes through the $x = 0$ points twice, there is a finite positive increment in the parallel kinetic energy. Furthermore, the approximate elastic bounce picture mentioned Sec. 3.2 implies that the initial and the final transverse kinetic energy should be comparable, so the increase of the total kinetic energy, i.e., $K_f - K_i \approx (M/m)e_{y0}\Delta\xi_y\beta_A^2$ of Eq. (33) should appear predominantly in the parallel component of the kinetic energy.

We now come back to $M/m = 1800$ case. The kinetic energy curves for model-I are shown in Fig. 5a and those for model-II in Fig. 5b. The general trend of the steady increase and the eventual dominance of $K_\parallel$ for both cases are qualitatively similar to the corresponding $M/m = 20$ case discussed earlier. Thus we have some qualitative understanding of the kinetic energy here, with the understanding that the test electron is moving with its gyro-radius reduced by about a factor of 90 and the corresponding gyro-period increased by a similar factor.

We summarize here our single test-particle simulation result for the physical mass ratio case. The SLAMS motivated parameters used are as follows. The Alfvèn speed is $v_A = 30km/s$ which is based on the ambient number electron density $n_0 = 2.2/\mathrm{cm}^3$ and $B_0 = 2\,\mathrm{nT}$. The jump of the magnetic field B_z is from $2\,\mathrm{nT}$ to $12\,\mathrm{nT}$ in the range of $\sim 100\,\mathrm{km}$. (This is twice of the half width, $D \sim 50\,\mathrm{km}$ used in this work). The speed of solar wind relative to the shock is $v^{pl} = 7v_A \sim 210\,\mathrm{km/s}$. The proton temperature of the plasma is $T_p = m_p c_s^2 = 50\,\mathrm{eV}$, where the speed of sound $c_s = 70\,\mathrm{km/s} \approx 2.3v_A$. Assuming the equality of the electron temperature and the proton temperature leads to $T_e = 50\,\mathrm{eV}$ or $v_e = 140v_A = 4200\,\mathrm{km/s}$, which serves as the source of the high speed test-electrons. For a test electron moving head-on toward the shock, the initial kinetic energy is $K_0 \sim 55\,\mathrm{eV}$, and the final electron energy is $K_f = (G_{II} - 1)K_0 \sim 550\,\mathrm{eV}$. Here the energy gain factor used was $G_{II} \sim 11$. The kinetic energy gain is due to with the work done by the dynamo field $E_{y0} = v^{pl}B_{z0} = 7v_A \times 2\,\mathrm{nT} \sim 0.42\,\mathrm{V/km}$, over a y-range of $\sim 1300\,\mathrm{km}$. During the y-drift, the test electron has completed about 650 cycles of gyration.

For $M/m = 1800$ case, i.e. the physical case, the factor cot 88.3° which enters in the gain factor expression of Eq. (34), is numerically close to the

physical ratio $(m_e/m_p)^{1/2}$. We introduce a parameter $\kappa = \cot\theta/\sqrt{m_e/m_p}$, so that gain factor can be written in the following manner.

$$\begin{aligned} G^{\rm phy} &= 1 + 4\left(\frac{u^{pl}}{\cos\theta u_{x0}}\right)^2 = 1 + 4\frac{m_p}{m_e}\left(\frac{\kappa v^{pl}}{v_{0x}}\right)^2 \\ &\approx 1 + \frac{2m_p v_{sh}^2}{T_e} = 1 + 2\left(\frac{v_{sh}}{c_s}\right)^2 \kappa^2. \end{aligned} \tag{39}$$

In the third step, the velocity of shock with respect to the plasma medium is introduced, where $v_{sh} = -v_{pl}$, and the electron temperature is given by $T_e = (1/2)mv_{0x}^2$. In the last step, c_s is the speed of sound in the plasma. For the physical case, $\kappa = \cot\ 88.3^\circ/\sqrt{m_e/m_p} \sim 0.8$, which is relatively close to unity as is expected from the discussion above. Following serves as a consistency check: $G^{\rm phy} = 1 + 2(210/70)^\times 0.8^2 \approx 11.2$.

A word of caution is in order here. The expression of gain factor given in Eq. (39) is obtained based on the set of specific values of n_0, B_0, B_1 v_{sh}, and T_e provided by the SLAMS data. The present model is formulated in terms of following dimensionless parameters: b_1, d, u^{pl}, u_{x0} and m/M. We defer the investigation of the dependence of the gain factor on these parameters to the future.

The ultrarelativistic acceleration of nonthermal, fast ions that cross the shock front many times was discussed with theory and simulations in Refs. [15, 16, 17]. In the Appendix, we apply this relativistic theory to electrons to obtain relativistic energy gain per gyro-period and gyro-averaged energy increase rate. Also, we show that particle momentum parallel to the magnetic field always goes up in each gyro-period, which is valid for any propagation angle. Unlike the discussion in the main text, in the Appendix these energy gain quantities are analyzed in the frame, where the plasma is at rest in the upstream region, and the shock is moving toward the plasma.

4 Energy gain factor on a fixed energy shell

This section we present the dependence of the energy gain factor on the polar and azimuthal angles of the velocity vector of initial electrons on a fixed energy shell. This is to show that a substantial part of the shell acquires energies over one-half of the maximum energy.

Consider a set of electrons which are uniformly distributed on the energy shell in plasma rest frame ("pr") of the solar wind. The direction of each

of electron initial velocity vectors is specified by a polar angle θ_{pr} measured from the solar wind velocity, and an azimuthal angle ϕ_{pr} defined in the y-z-plane. The Cartesian components of the initial velocity vector is defined by

$$\begin{aligned} u_x &= -u_{pr}\cos\theta_{pr} + u^{pl} \\ u_y &= -u_{pr}\sin\theta_{pr}\ \cos\phi_{pr} \\ u_z &= -u_{pr}\sin\theta_{pr}\ \sin\phi_{pr}. \end{aligned} \tag{40}$$

For the reference case we use the values $u^{pl}v_A = -210\,\mathrm{km/s}$ and $u_{pr}v_A = 4200\,\mathrm{km/s}$. We consider $-1 \le \cos\theta_{pr} \le 1$ and $0 \le \phi_{pr} \le 2\pi$ For the present fixed energy shell study, $16 \times 8 = 128$ grid points. For the variable ϕ_{pr}, the grid begins with $\phi_{pr} = 0$. There are 16 equal spaced points with $\delta\phi_{pr} = 25°$. For θ_{pr}, the grid-point begins at $\cos\theta_{pr} = 1$. There are 8 equal spacing points with $\delta\cos\theta_{pr} = 0.25$.

Figure 6 shows how the energy multiplication factor varies as a function of ϕ_{pr} for various polar angle θ_{pr}. As shown in Fig. 6, there are two peaks. One is about $\phi = 0°$ and the other about $\phi = 180°$. Both cases correspond to the situation where the initial u_y is large and the initial u_z is small. So the projected gyro-radius in the x-y-plane is relatively large. With the large gyro-radius, the drift along the y-direction near $x = 0$ can be extended over a relatively long range in y and in turn a relatively large energy multiplicative factor is obtained. This explains the presence of the two peaks. Moreover, analysis on Fig. 6 indicates that about 1/3 of electrons on the fixed energy shell of interest has a multiplicative factor greater than 10. In other words, there is a significant fraction of the electrons on this fixed energy shell, being accelerated to an energy, which is over half of the maximum energy.

5 Summary and conclusions

In this work, based on Lorentz force law we investigated the acceleration of high speed test-electrons, as they enter into the region of a quasi-normal shock. The shock has the basic upstream field components: B_z with a ramp toward the shock front and a constant $B_x = B_0\cos\theta$ where $\cos\theta \ll 1$. In the shock frame, there is the dynamo field $E_{y0} = -v^{pl}B_{z0}$. In addition, due to nonlinear effects, self-consistency requires local fields E_x and B_y. In our numerical work, we have considered two structures: model-I consists of the

basic upstream field components together with the dynamo field, model-II includes also the local fields.

Parameters of the shock are chosen to be comparable to the SLAMS (short large amplitude magnetic structure) data, except for θ which is tuned to optimize the final energy. A priori one expects that the behavior of a trajectory is sensitive to precise initial condition chosen. We circumvent this difficulty by breaking up our investigation in two stages. In the first stage, our fine-tuning procedure allows us to work with specific initial conditions, which lead to events with maximum energy. We find the optimal angle decreases as the proton to electron mass ratio increases, which has been associated with the M/m scale breaking. At the second stage, we performed a fixed energy shell analysis, which alleviates the fine-tuning restriction.

We have developed a physical picture and a formula for the trapped range in the y-direction before the gyrating electron is reflected away from the shock front. The analytic expression derived has the form: $G = G_\theta$, which correlates the optimal energy gain to the quasi-normal angle, which is the angle between the shock velocity and the upstream magnetic field, with one parameter $\overline{f}$. With the appropriate choice of the parameter value, this relation works to within a few percents.

Based on the quasi-normal approximation, we have demonstrated for model-I the staircase pattern in the temporal evolution of the parallel kinetic energy where the jump occurs at every step as the $x = 0$ line is crossed. For model-II, a modified staircase pattern with spikes at the ramp, with a positive increase of parallel component in each gyro-cycle during the y-drift is still expected. In the appendix, it is shown that this positivity condition holds in the relativistic regime also. Based on an "elastic bounce" picture, we argue that the eventual dominance of the parallel kinetic energy in the final state is expected. We have carried out a fixed energy shell simulation showing that electrons from a substantial fraction of the shell have acquired energies, which are over one-half of the maximum energy.

To sum up, based on the shock front orbital drift picture constructed, we show the details of how the electrons are accelerated in the shock through a long drift in y accompanying a large number of crossings the shock front. As a result, the electrons pick up an order of magnitude of energy in the shock frame and are ejected with all the energy gain in the parallel kinetic energy. Thus, the energized electrons are ejected along the magnetic field with small pitch angles into the foreshock. This beam of electron electrons will typically drive either electron plasma was unstable or the electron firehose instability

depending on the details of the foreshock plasma.

Acknowledgments

This work is supported in part by the NSF-Focus Seed Funding Grant, NSF Grant ATM-0229863, and by the US-Japan Joint Institute for Fusion Theory.

Appendix: Comparison with the relativistic model by Usami *et al.*

So far we have confined our investigation in the rest frame of the shock. We have used quasi-normal approximation and the nonrelativistic kinematics. Here, we apply the theory of acceleration of relativistic ions [15, 16, 17] to electrons to understand this mechanism in a more general context. As in Sec. 3 and Sec. 4, we consider electrons crossing the shock front many times. We, however, use relativistic kinematics. The results are valid for any finite propagation angle.

Here, for comparison, we discuss the particle motion and energization in the laboratory frame, where the plasma is at rest in the upstream region. In the wave frame, E_y is constant in time and space. However, in the laboratory frame, it depends on x and t; $E_y = 0$ in the upstream region while $E_y > 0$ in the shock wave.

5.0.1 Energy jump and gyro-averaged increase rate of the Lorentz factor

Energetic electrons crossing the shock front several times gain energy from E_y in the shock wave; while they are in the upstream region, the kinetic energies are constant. We can therefore obtain the amount of energy increase per one gyro-period by calculating $-e\int E_y v_y dt$ along the orbit in the shock wave. Suppose that the particle goes in the shock wave at $t = t_{\rm in}$ and goes out to the upstream region at $t = t_{\rm out}$, the increase in the electron Lorentz factor, $\delta\gamma = -e\int E_y v_y dt/(m_e c^2)$, is given as [15]

$$\delta\gamma = \frac{2q_e p_{1\perp} E_{1y}}{m_e^2 c^2 \Omega_{e1}} \sin\left(\frac{|\Omega_{e1}|(t_{\rm out} - t_{\rm in})}{2\gamma}\right). \tag{A1}$$

Here, q_e is the electron charge, and Ω_e is the nonrelativistic electron gyro-frequency ($q_e/\Omega_e > 0$); the subscript 1 refers to quantities in the strong-field region.

The energy jump becomes the maximum when

$$|\Omega_{e1}|(t_{\rm out} - t_{\rm in})/(2\gamma) = \pi/2. \tag{A2}$$

Equation (A1) gives the increase in the perpendicular kinetic energy while the particle is in the shock wave. However, substantial part of it is converted to the parallel energy when the particle crosses the shock front.

The energy increase rate averaged over gyro-period can also be estimated [16]. If the fast particle spends most of the time in the upstream region in each gyro-period, the acceleration time, $t_{\rm out} - t_{\rm in}$, would be much shorter than the gyro-period, which is approximately given by the gyro-period $2\pi\gamma/|\Omega_{e0}|$. Then, the time rate of change of γ of a particle accelerated many times by a stationary shock wave is given as

$$\frac{d\gamma}{dt} = \frac{g}{\pi}\frac{v_{\rm sh}}{c}|\Omega_{e0}|, \tag{A3}$$

where g is a numerical factor smaller than unity,

$$g = \frac{v_{1\perp}}{c}\left(1 - \frac{B_{z0}}{B_{z1}}\right)\left(1 - \frac{B_{x0}^2}{2B_{z1}^2}\right)\sin\left(\frac{|\Omega_{e1}|(t_{\rm out} - t_{\rm in})}{2\gamma}\right). \tag{A4}$$

Here, $d\gamma/dt$ was averaged over the gyro-period $2\pi\gamma/|\Omega_{e0}|$, and it was assumed that $B_{z1} > B_{x0}$.

For the case of Eq. (A2), time averaging should be made with half of the gyro-period at the upstream side $\sim \pi\gamma/|\Omega_{e0}|$. If we neglect the time which electron spends in the shock wave, since the gyro-period in the shock wave should be much shorter than that in the upstream region, then the energy increase rate should be about twice the rate given in Eq. (A3).

5.0.2 Relativistic increase in parallel momentum per cycle

Here, we will show that the parallel momentum of an energetic electron increases when it crosses a thin shock transition region [17].

We consider an energetic electron such that its gyro-radius is much greater than the width of the shock transition region. Thus, when we discuss its motion, the magnetic field profile can be approximated by a step function; from the upstream field $\boldsymbol{B}_0$ to the field in the shock wave $\boldsymbol{B}_1$. Both $\boldsymbol{B}_0$ and $\boldsymbol{B}_1$ are assumed to be constant;

$$\boldsymbol{B}_1 = B_1\left(\cos\theta_1, 0, \sin\theta_1\right)$$

with $B_1 > B_0$ and $\theta_1 > \theta_0$. Here, we neglect the y-component of $\boldsymbol{B}$, because it has finite values only in the narrow transition layer.

From the equation of motion, we have

$$\frac{d(\boldsymbol{p}\cdot\boldsymbol{B})}{dt} = \boldsymbol{p}\cdot\frac{d\boldsymbol{B}}{dt} + q_e\boldsymbol{E}\cdot\boldsymbol{B}. \tag{A5}$$

In the following, we will neglect the second term on the right-hand side of Eq. (A5), because the parallel electric field is weak in magnetohydrodynamic waves. The effect of perpendicular electric field is, however, retained.

Noting that the magnetic field profile is a step function, we integrate Eq. (A5) over time from the time immediately before $t = t_{\rm in}$ to the time immediately after $t = t_{\rm out}$. It gives

$$\left[p_{0\parallel}(t_{\rm out}) - p_{0\parallel}(t_{\rm in})\right] B_0 = [\boldsymbol{p}(t_{\rm in}) - \boldsymbol{p}(t_{\rm out})] \cdot (\boldsymbol{B}_1 - \boldsymbol{B}_0)\,. \tag{A6}$$

When the energetic particle crosses the narrow transition layer of the shock wave, $\boldsymbol{p}_\parallel$ and $\boldsymbol{p}_\perp$ change stepwise owing to the change in the magnetic field from $\boldsymbol{B}_0$ to $\boldsymbol{B}_1$, even though $\boldsymbol{p}$ is continuous.

Also, because $q_e \boldsymbol{E} \cdot \boldsymbol{B}$ is negligible, $p_{1\parallel}(t)$ is constant during the time from $t = t_{\rm in}$ to $t = t_{\rm out}$. We therefore have $\boldsymbol{p}(t_{\rm in}) - \boldsymbol{p}(t_{\rm out}) = \boldsymbol{p}_{1\perp}(t_{\rm in}) - \boldsymbol{p}_{1\perp}(t_{\rm out})$. Then, noting that $\boldsymbol{p}_{1\perp} \cdot \boldsymbol{B}_1 = 0$, we have the change in the parallel momentum, $\delta p_\parallel = p_{0\parallel}(t_{\rm out}) - p_{0\parallel}(t_{\rm in})$, as

$$\delta p_\parallel = [\boldsymbol{p}_{1\perp}(t_{\rm out}) - \boldsymbol{p}_{1\perp}(t_{\rm in})] \cdot \boldsymbol{B}_0 / B_0. \tag{A7}$$

We introduce the unit vector $\boldsymbol{e}_{x'}$ in the direction perpendicular to $\boldsymbol{B}_1$ and to the y-axis; i.e., $\boldsymbol{e}_{x'} = \boldsymbol{e}_y \times \boldsymbol{B}_1 / B_1$ where $\boldsymbol{e}_y$is the unit vector in the y-direction. We then use the quantity

$$p_{1\perp x'} = \boldsymbol{p}_{1\perp} \cdot \boldsymbol{e}_{x'}, \tag{A8}$$

to put Eq. (A7) into the form

$$\delta p_\parallel = [p_{1\perp x'}(t_{\rm out}) - p_{1\perp x'}(t_{\rm in})] \sin(\theta_1 - \theta_0). \tag{A9}$$

With the aid of Eq. (A9), one can show that $\delta p_\parallel$ is always positive [17]. At the moment when the particle enters the shock region from the upstream region, the x component of the particle velocity must be smaller than the shock speed $v_{\rm sh}$. Also, when the particle goes out to the upstream region, v_x must be greater than $v_{\rm sh}$. Using momentum, we can express these as

$$p_{1\parallel}(t_{\rm in}) \cos\theta_1 + p_{1\perp x'}(t_{\rm in}) \sin\theta_1 < m_e \gamma(t_{\rm in}) v_{\rm sh}, \tag{A10}$$

$$p_{1\parallel}(t_{\rm out}) \cos\theta_1 + p_{1\perp x'}(t_{\rm out}) \sin\theta_1 > m_e \gamma(t_{\rm out}) v_{\rm sh}. \tag{A11}$$

Comparison of these inequalities leads to

$$p_{1\perp x'}(t_{\rm out}) > p_{1\perp x'}(t_{\rm in}), \tag{A12}$$

because $p_{1\parallel}(t_{\rm in}) = p_{1\parallel}(t_{\rm out})$ and $\gamma(t_{\rm out}) > \gamma(t_{\rm in})$. [The electric field E_y makes $\gamma(t_{\rm out})$ greater than $\gamma(t_{\rm in})$ [16]. Obviously, however, even when $\gamma(t_{\rm out}) = \gamma(t_{\rm in})$, the relation (A12) holds.] Because $\theta_1 > \theta_0$, it follows from Eqs. (A9) and (A12) that $p_\parallel$ always increases,

$$\delta p_\parallel = p_{0\parallel}(t_{\rm out}) - p_{0\parallel}(t_{\rm in}) > 0. \tag{A13}$$

This result is Eq. (27), given in Ref. [17].

References

[1] M. Takeda, N. Hayashida, K. Honda, *et al.*, Phys. Rev. Lett. **81**, 1163 (1998).

[2] K. Koyama, R. Petre, E. V. Gotthelf, *et al.*, Nature (London) **378**, 255 (1995).

[3] T. Tanimori, Y. Hayami, S. Kamei, *et al.*, Astrophys. J. Lett. **497**, L25 (1998).

[4] F. A. Aharonian, A. G. Akhperjanian, J. A. Barrio *et al.*, Astrophys. J. **539**, 317 (2000).

[5] R. Enomoto, T. Tanimori, T. Naito, *et al.*, Nature (London) **416**, 823 (2002).

[6] E. L. Chupp, H. Debrunner, E. Flückiger, *et al.*, Astrophys. J. **318**, 913 (1987).

[7] D. J. Forrest and E. L. Chupp, Nature (London) **305**, 291 (1983).

[8] S. R. Kane, E. L. Chupp, D. J. Forrest, G. H. Share, and E. Rieger, Astrophys. J. Lett. **300**, L95 (1986).

[9] J. P. Meyer, Astrophys. J. Suppl. **57**, 151 (1985).

[10] J. P. Meyer, Astrophys. J. Suppl. **57**, 173 (1985).

[11] Y. Ohsawa, Physica Scripta **T107**, 32 (2004).

[12] W. Horton and C. Chiu, Phys. Plasmas **11**, 1645 (2004).

[13] K. Stasiewicz, P. K. Shukla, G. Gustafsson, S. Buchert, B. Lavraud, B. Thide, and Z. Klos, Phys. Rev. Lett. **90**, 085002 (2003).

[14] K. Stasiewicz, M. Longmore, S. Buchert, P. K. Shukla, B. Lavraud, and J. Pickett, Geophys.. Res. Lett. **30**, 2241 (2003).

[15] S. Usami, H. Hasegawa, and Y. Ohsawa, Phys. Plasmas **8**, 2666 (2001).

[16] S. Usami and Y. Ohsawa, Phys. Plasmas **9**, 1069 (2002).

[17] S. Usami and Y. Ohsawa, Phys. Plasmas **11**, 918 (2004).

[18] N. Bessho and Y. Ohsawa, Phys. Plasmas **9**, 979 (2002).

[19] J. Adlam and J. Allen, Phil. Mag. **3**, 448 (1958).

[20] D. A. Tidman nd N. A. Krall, "Shock waves in collisionless plasmas," (Wiley-Interscience, Wiley & Sons, Inc, New York, 1971) chapters 3-4.

[21] M. F. Thomsen, et al., J. Geophys. Res. **92**, 2305 (1987).

[22] C. C. Goodrich and J. D. Scudder, J. Geophys. Rev. **89**, 6654 (1984).

[23] R. A. Cairns, J. Geophys. Res. **91**, 7134 (1986).

[24] C. C. Goodrich and J. D. Scudder, J. Geophys. Rev. **91**, 7135 (1986).

[25] F. C. Jones and D. C. Ellison, J. Geophys. Res. **92**, 11205 (1987).

[26] V. D. Shapiro and Defne Ucer, Planetary and Space Sci. **51**, 665 (2003).

[27] Y. Ohsawa, Phys. Fluids **29**, 1844 (1986).

[28] T. Kakutani, H. Ono, T. Taniuti and C. C. Wei, J. Phys. Soc. Jpn. **24**, 1159 (1968).

[29] H. Washimi and T. Taniuti, Phys. Rev. Lett. **17**, 996 (1966).

[30] T. Kakutani and H. Ono, J. Phys. Soc. Jpn. **26**, 1305 (1969).

[31] S. P. Gary and K. Nishimura, Phys. Plasmas **10**, 3571 (2003).

[32] Y. Ohsawa, J. Phys. Soc. Jpn. **57**, 929 (1988).

FIGURE CAPTIONS

FIG. 1. The $M/m = 1800$ case. (a) Projected trajectory in the x-y-plane of a gyrating electron, from the collision of a high-β plasma with a shock near $x = 0$. The shock parameters are based on the reported event from SLAMS data: $B_{\max}/B_0 = 6$, $D = 50\,\mathrm{km} \sim 0.3c/\omega_{pi}$, except for the oblique angle, which is chosen to be at $\theta = 88.3°$. Zoom-in views: (b) after the transient region $0 < x < d$ near the exit end, (c) at the midway in the y-drift region, and (d) before the transient region $0 < x < d$ near the start of the y-drift.

FIG. 2. The $M/m = 20$ case. (a) Projected trajectory in the x-y-plane of a gyrating electron, from the collision of a high-β plasma with a shock near $x = 0$. The shock parameters are based on the reported event from SLAMS data: $B_{\max}/B_0 = 6, D = 50\,\mathrm{km} \sim 0.3c/\omega_{pi}$, except for the oblique angle, which is chosen to be at $\theta = 88.7°$. Zoom-in views: (b) transient region near the exit end, (c) at the midway in the y-drift region, and (d) the transient region near the start of the y-drift.

FIG. 3. Typical electron gyration orbits in an analytic model, applicable when electron gyro-radius $r_e \gg c/\omega_{pi}$. The electron follows the path: BPAB'P' with a counterclockwise gyration.

FIG. 4. $M/m = 20$ case: Plots (a) and (b) illustrate the angular dependence of the G-factor. G_θ is indicated by a curve, G_{II}, by cross-points. Plot (c) shows the angular dependence of the total number of gyro-cycles in the y-drift region. $M/m = 1800$ case: Plots (d) and (e) have the same meaning as the corresponding plots of (a) and (b), except that they are now for $M/m = 1800$ case. Plot (f): Total number of gyro-cycles in the y-drift region for 3 cases considered: $M/m = 20$, 200 and 1800 based on model-II, where each case is evaluated at its respective optimal angle.

FIG. 5. Plots (a) to (d): Temporal evaluation of the total, $\|$, and transverse kinetic energies. (a) $M/m = 1800$, model-I. (b) $M/m = 1800$, model-II. (c) $M/m = 20$, model-I. (d) $M/m = 20$, model-II, where $K_\|^I$ is the curve of model-I in (c) is superposed for comparison. Plots (e) and (f): Zoom-in view of x vs. t for $M/m = 20$. (e) model-I

and (f) model-II. Plots (g) and (h): The corresponding zoom in view of $K_{\|}$ vs. t. The thick vertical lines are at the times when electron enters the shock region, labeled by (P, P' in Fig. 3) and the thin vertical are when electrons leave the shock region. Notice the staircase pattern in (g) and the modified staircase pattern with spikes in (h).

FIG. 6. The azimuthal angular dependence ϕ_{pr} of the energy multiplication factor $G_e = K_f/K_i$ for a set of electrons on a fixed energy shell at various polar angles, where $\cos\theta_{pr} = 1$ (heavy-solid), 0.75 (light-solid), 0.5 (dash), 0 (long-dash), -0.5 (long-dash-short-dash), -0.75 (short-dash). The polar and the azimuthal angles are defined in the text, see Eq. (40).

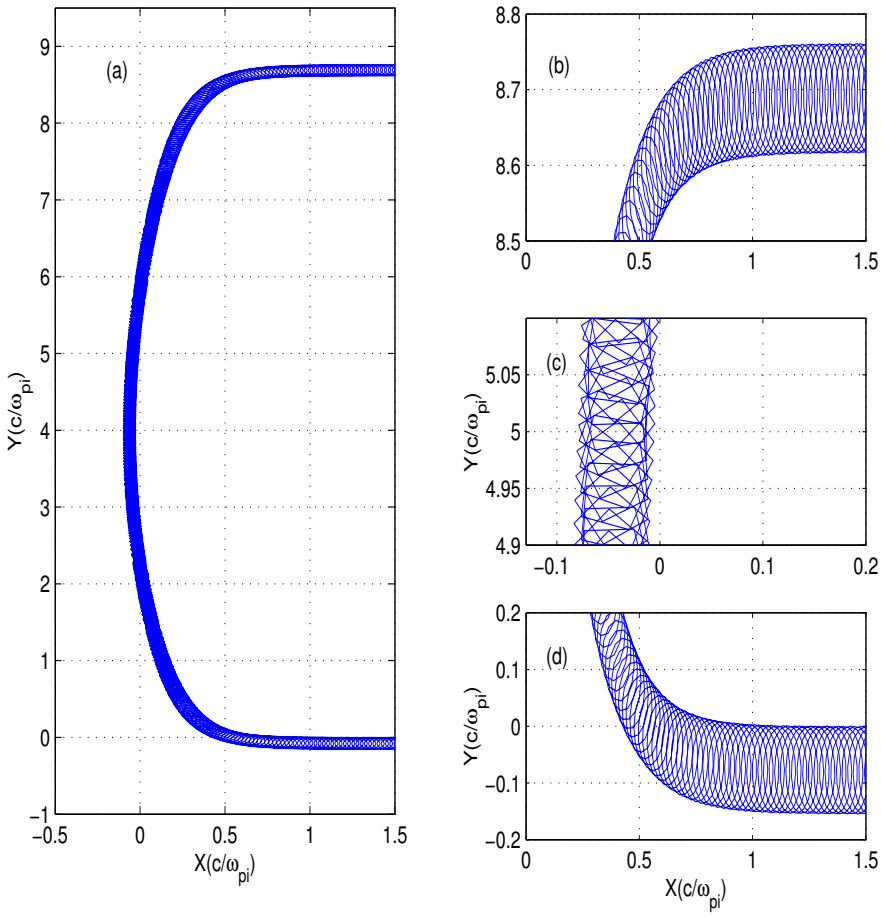

Fig 1.

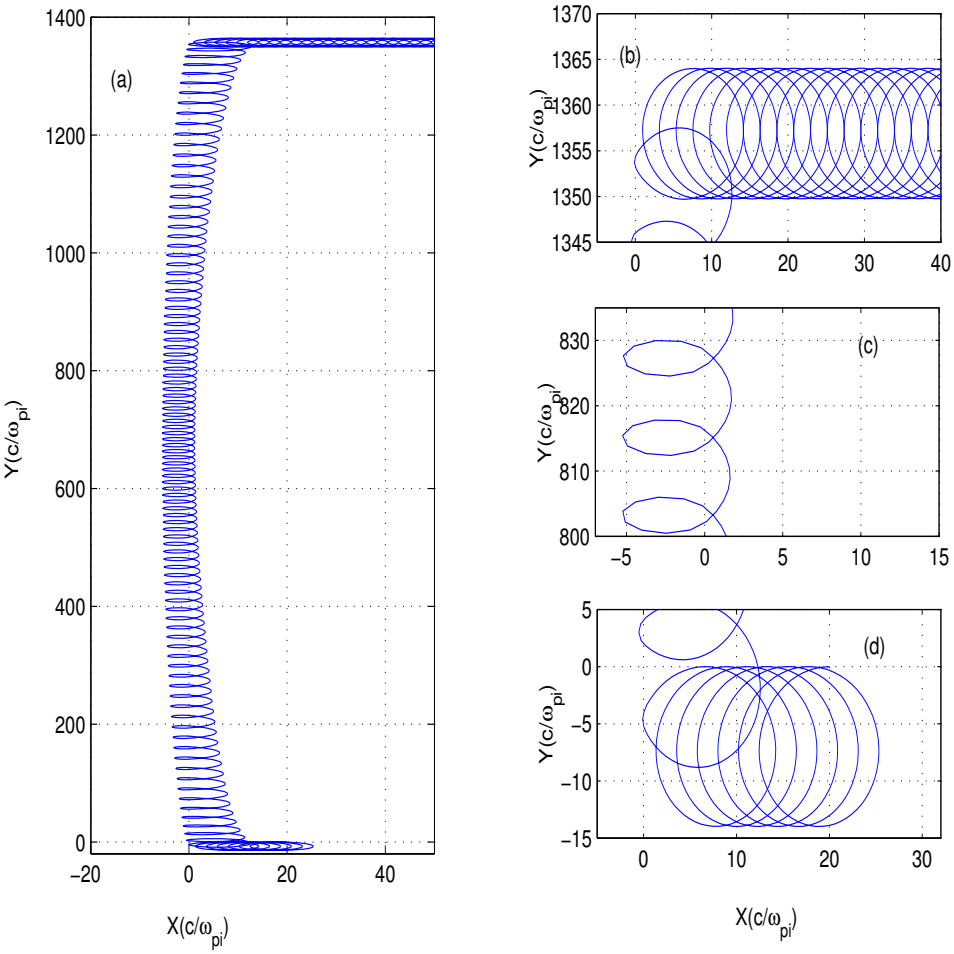

Fig 2.

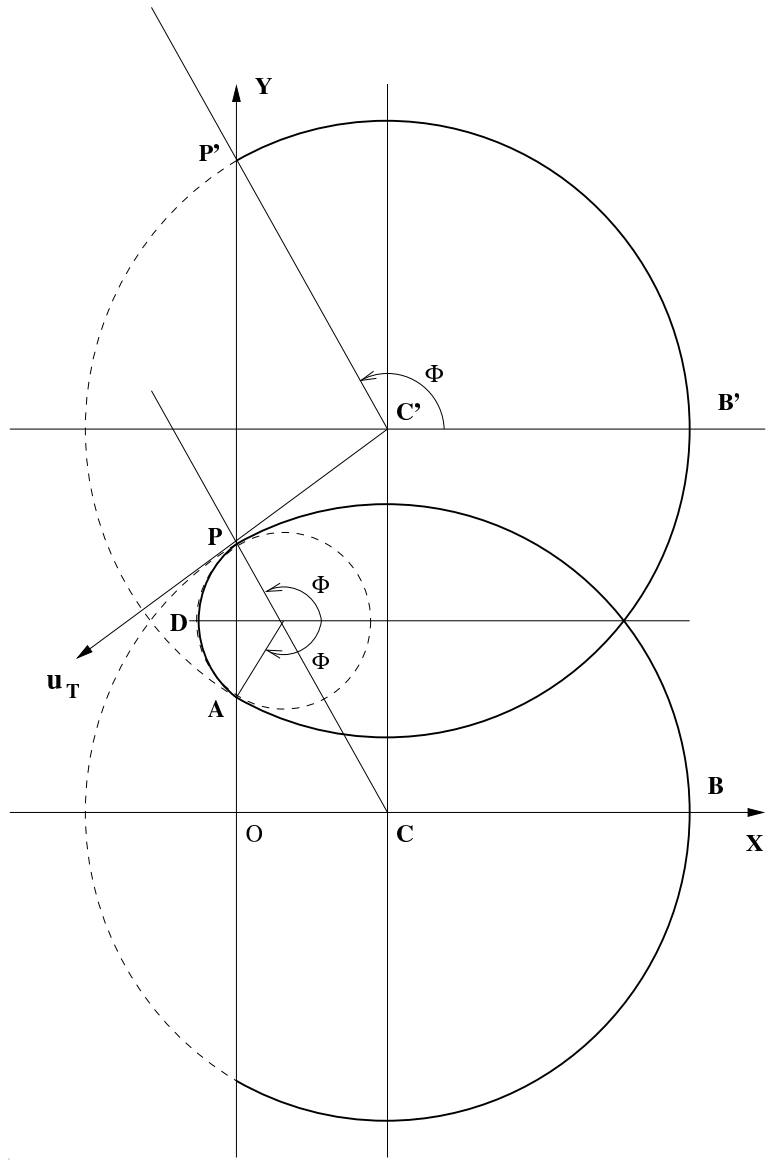

Fig 3.

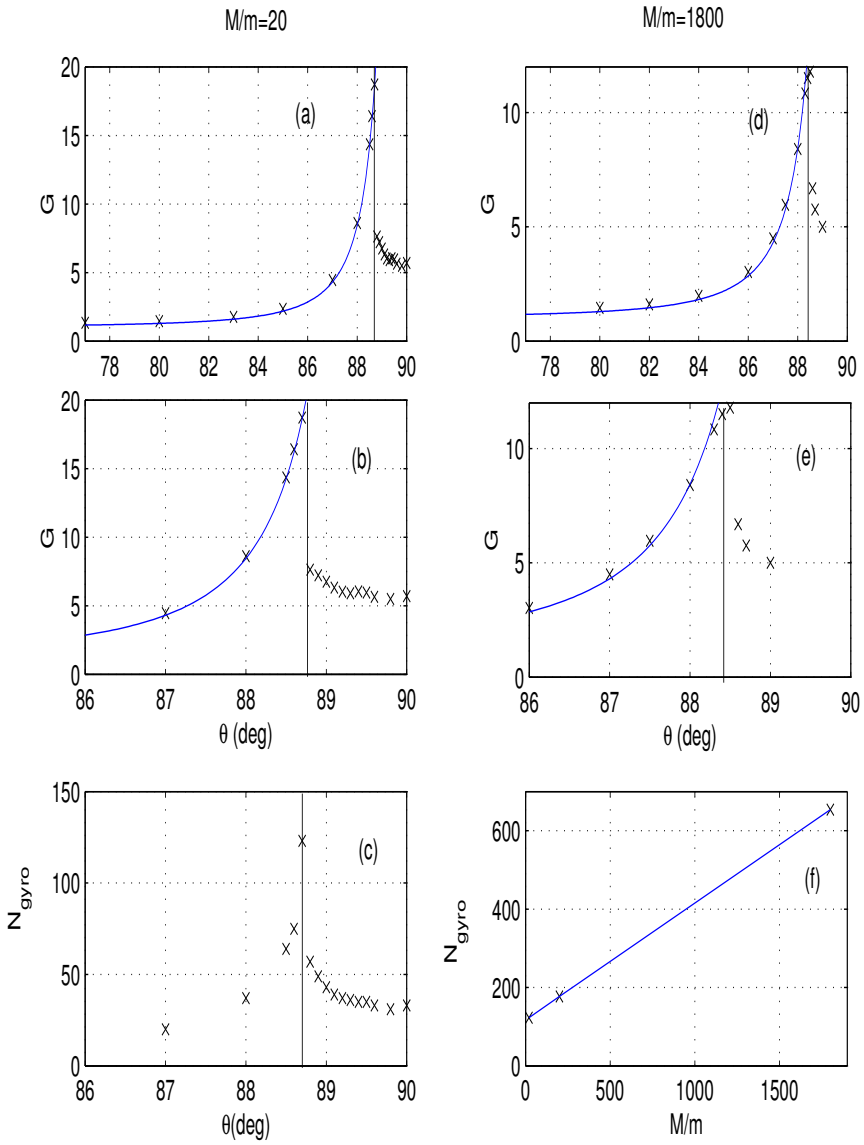

Fig 4.

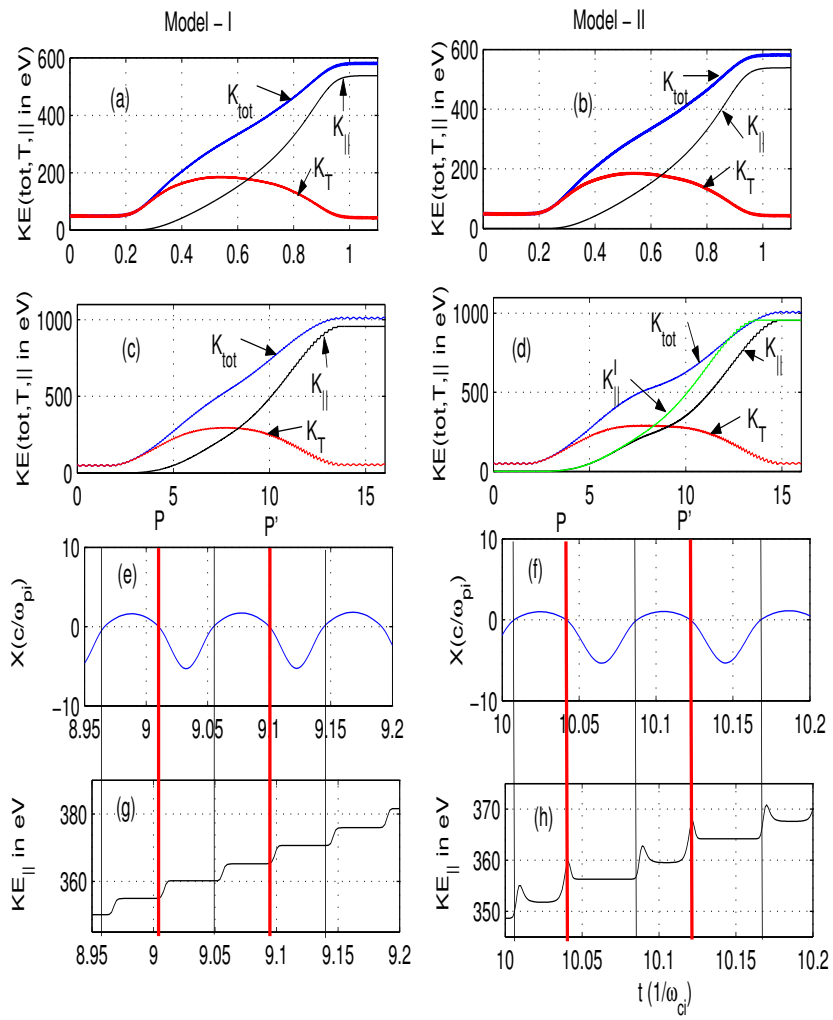
Model – I
Model – II
KE(tot,T,|| in eV)
(a)
(b)
(c)
(d)
(e)
(f)
(g)
(h)
K_tot
K_||
K_T
K^I_||
P
P'
X(c/ω_pi)
KE_|| in eV
t (1/ω_ci)

Fig 5.

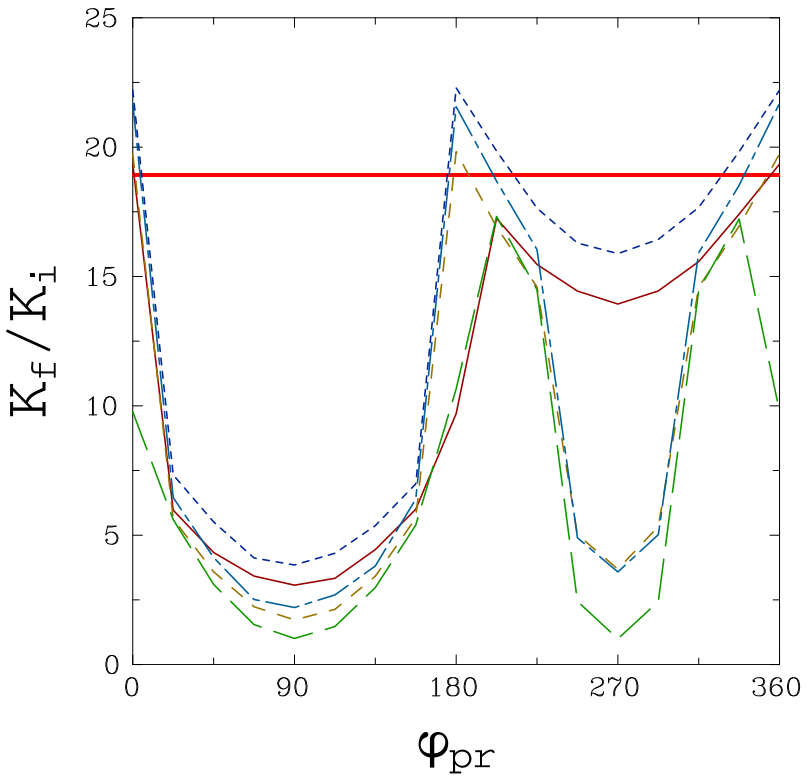

Fig 6.